Supporting Information

Low Temperature Structures and Magnetic Interactions in the Organic-based Ferromagnetic and Metamagnetic Polymorphs of Decamethylferrocenium 7,7,8,8-Tetracyano-*p*-quinodimethanide, $[FeCp^*_2]^{\cdot+}[TCNQ]^{\cdot-}$

Saul H. Lapidus, Peter W. Stephens, Maria Fumanal, Jordi Ribas-Ariño, Juan J. Novoa, Jack G. DaSilva, Arnold L. Rheingold, Joel S. Miller

Figure S1. High-resolution synchrotron powder diffraction data (black dots) and Rietveld fit (red line) of the data for $\mathbf{MM_{LT}}$ polymorph of $[FeCp^*_2][TCNE]$ at 17 K. The lower green trace is the difference, measured – calculated, plotted to the same vertical scale. The center inset is a magnified view of the region from 11.5 to 12°, illustrating noise in the data due to large grain size and poor statistics in the powder data set, a consequence of insufficient rotation of the sample during data collection. The upper-right inset is a vertically magnified view of the region above 12°.

Figure S2. High-resolution synchrotron powder diffraction data (black dots) and Rietveld fit (red line) of the data for $\mathbf{MM_{RT}}$ polymorph of $[FeCp^*_2][TCNE]$ at 295 K. The lower green trace is the difference, measured – calculated, plotted to the same vertical scale. The inset is a vertically magnified view of the region above 14°.

Figure S3. High-resolution synchrotron powder diffraction data (black dots) and Rietveld fit (red line) of the data for **FO** polymorph of $[FeCp^*_2][TCNE]$ at 19 K. The lower green trace is the difference, measured – calculated, plotted to the same vertical scale. The inset is a vertically magnified view of the region above 14°.

Figure S4. Powder X-ray diffraction patterns of **MM** in a limited angular range, showing the differences among the three **MM** phases. Red lines are Rietveld refinements as discussed in the text. Patterns at 215 and 60 K show clear two-phase coexistence.

Figure S5. Nearest neighbor parallel chains **I**, **II**, **II'**, **III**, **III'**, **IV**, and **V** present in the 19-K structure of **FO**.

Figure S6. Nearest neighbor in-registry **I-II** (and **I-II'**), and out-of-registry **I-III** (and **I-III'**), **I-IV**, and **I-V** parallel chains present in the 19-K structure of **FO**, and the key intra- and interchain separations (Å).

Figure S7. Nearest neighbor parallel chains **I**, **II**, **II'**, **III**, **III'**, **IV**, and **IV'** present in the 17-K structure of $\mathbf{MM_{LT}}$.

Figure S8. Nearest neighbor out-of-registry **I-II** (and **I-II'**) and **I-III** (and **I-III'**) as well as in-registry **I-IV** (and **I-IV'**) parallel chains present in the 17-K structure of $\mathbf{MM_{LT}}$, and the key intra- and interchain separations (Å).

Figure S9. RAS(X, 2, 2; n1, n2, n3) space includes all possible configurations contained in RAS2 and all 1h, 1p, 1h1p, 2h, 2p, 2h1p, 1h2p and 2h2p type of excited configurations considering the RAS1 and RAS3 spaces.

Figure S10. Active orbitals of the RAS(34,2,2;15,3,18) space used to compute the *J* values for the $[FeCp^*_2]^{\bullet+}$•••$[TCNQ]^{-\bullet}$ pairs. The 3 orbitals placed inside red squares are the orbitals included in the RAS2 subspace, while the 15 above are the RAS1 and the 18 below the RAS3 subspaces. As shown in Figure S9, the orbitals and electrons included in RAS2 give rise to the same type of full-CI expansion as in a Complete Active Space (CAS) calculation.

Figure S11. Active orbitals of the RAS(34,2,2;16,2,14) space used to compute the *J* values for the $[TCNQ]^{-\bullet}$•••$[TCNQ]^{-\bullet}$ pairs. The 3 orbitals placed inside red squares are the orbitals included in the RAS2 subspace, while the 16 above are the RAS1 and the 14 below the RAS3 subspaces. As shown in Figure S9, the orbitals and electrons included in RAS2 give rise to the same type of full-CI expansion as in a Complete Active Space (CAS) calculation.

Figure S12. Active orbitals of the RAS(34,2,2;14,4,22) space used to compute the *J* values for the $[FeCp^*_2]^{\bullet+}$•••$[FeCp^*_2]^{\bullet+}$ pairs. The 4 orbitals placed inside red squares are the orbitals included in the RAS2 subspace while the 14 above are the RAS1 and the 22 below the RAS3 subspaces. As shown in Figure S9, the orbitals and electrons included in RAS2 give rise to the same type of full-CI expansion as in a Complete Active Space (CAS) calculation.

Figure S13. Magnetic topologies of [FeCp*$_2$][TCNE] and **FO** and **MM$_{LT}$** polymorphs of [FeCp*$_2$][TCNQ]. A unit cell is depicted by the dashed blue lines.

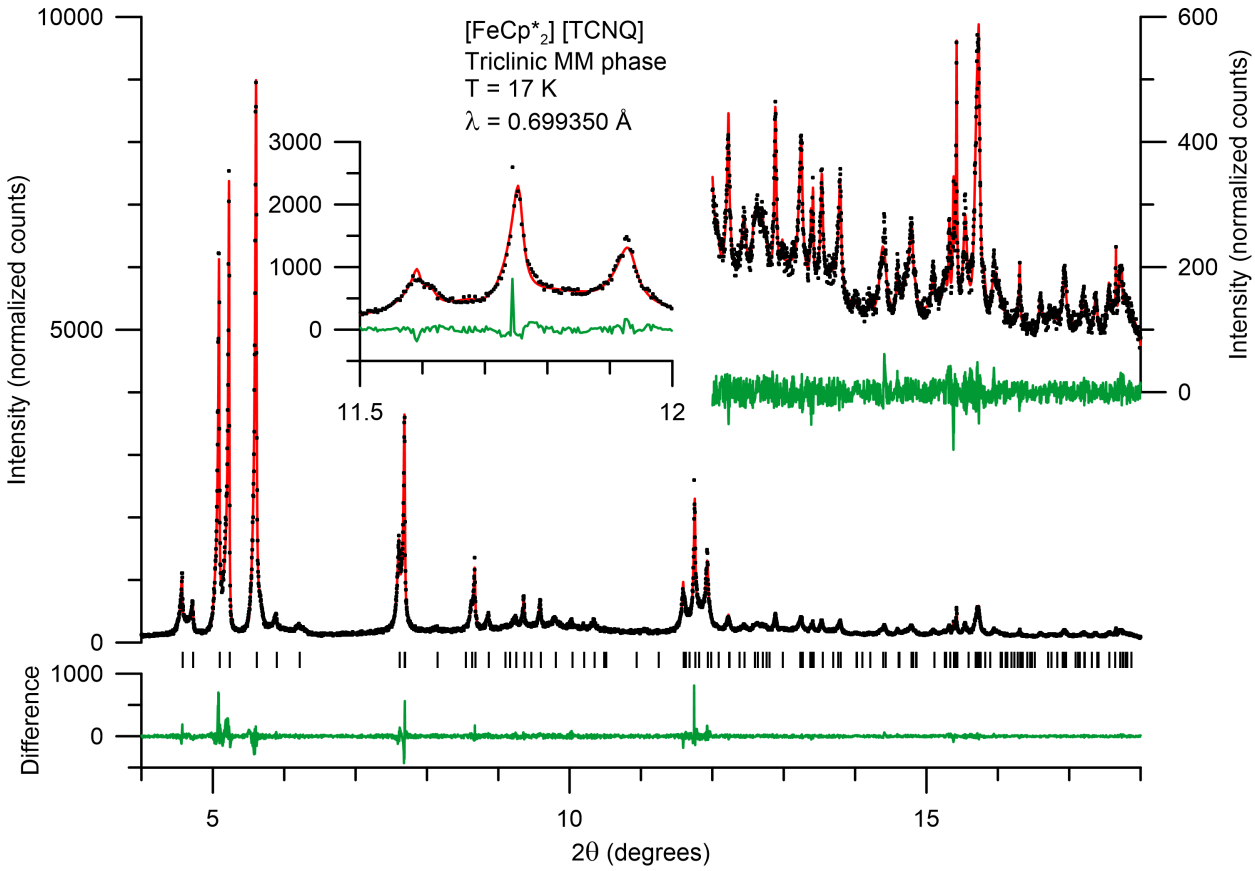

Figure S1. High-resolution synchrotron powder diffraction data (black dots) and Rietveld fit (red line) of the data for **MM$_{LT}$** polymorph of [FeCp*$_2$][TCNE] at 17 K. The lower green trace is the difference, measured – calculated, plotted to the same vertical scale. The center inset is a magnified view of the region from 11.5 to 12°, illustrating noise in the data due to large grain size and poor statistics in the powder data set, a consequence of insufficient rotation of the sample during data collection. The upper-right inset is a vertically magnified view of the region above 12°.

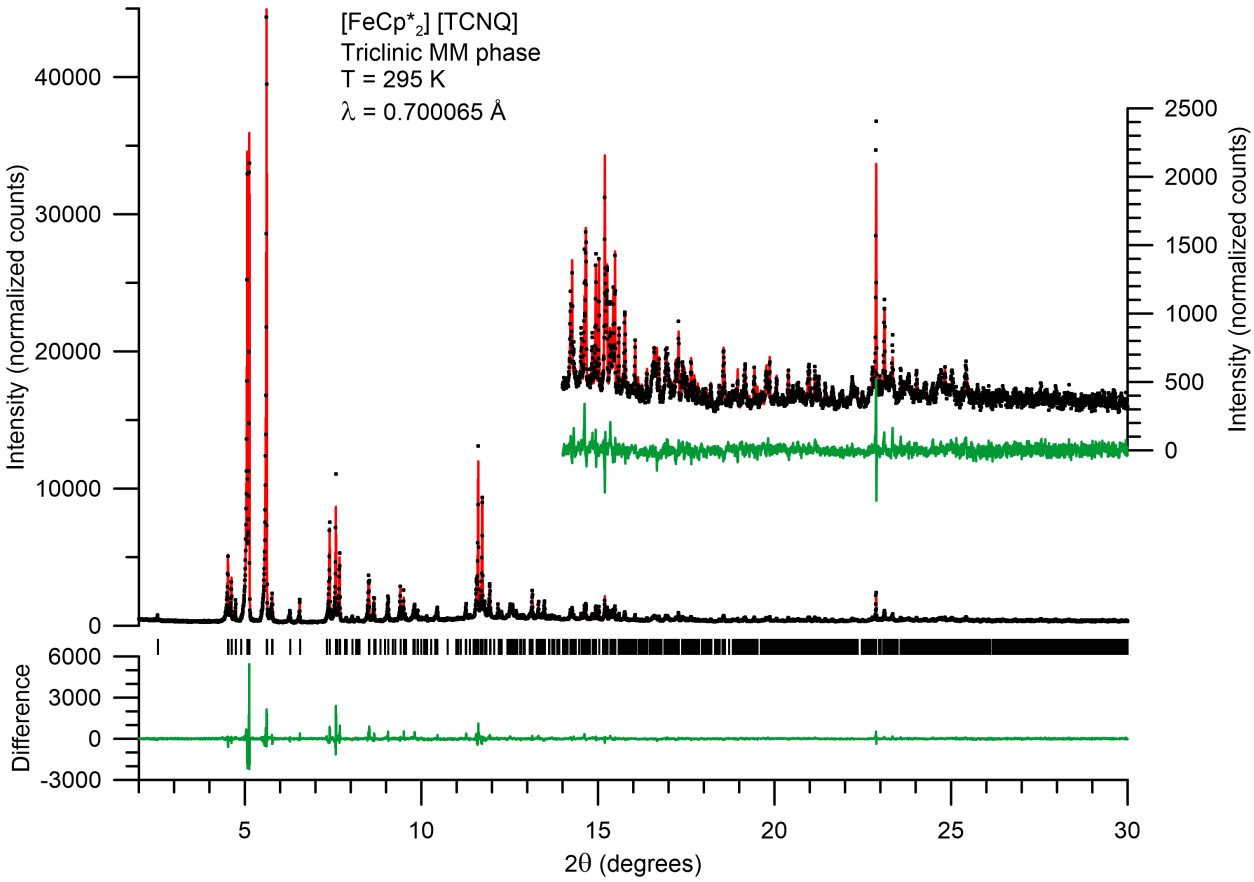

Figure S2. High-resolution synchrotron powder diffraction data (black dots) and Rietveld fit (red line) of the data for **MM$_{RT}$** polymorph of [FeCp*$_2$][TCNE] at 295 K. The lower green trace is the difference, measured – calculated, plotted to the same vertical scale. The inset is a vertically magnified view of the region above 14°.

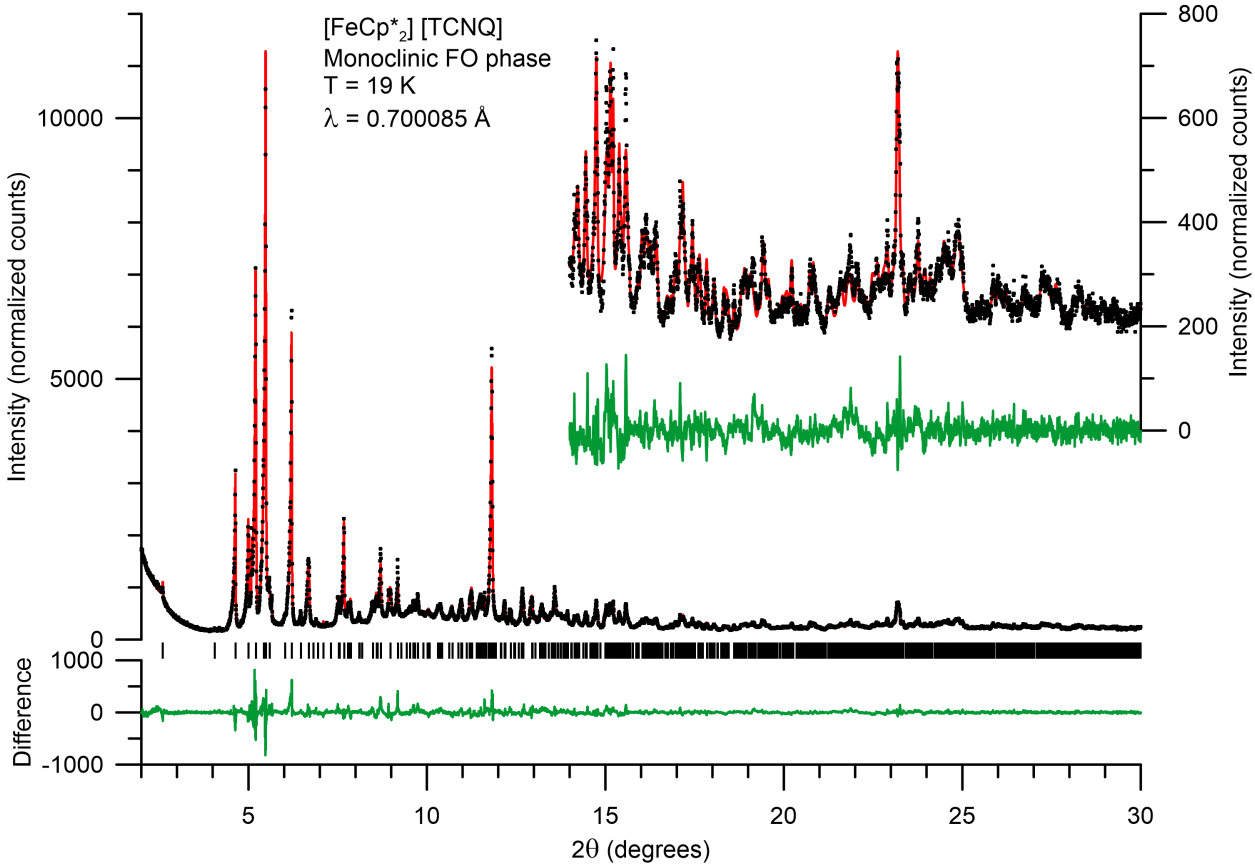

Figure S3. High-resolution synchrotron powder diffraction data (black dots) and Rietveld fit (red line) of the data for **FO** polymorph of [FeCp*$_2$][TCNE] at 19 K. The lower green trace is the difference, measured – calculated, plotted to the same vertical scale. The inset is a vertically magnified view of the region above 14°.

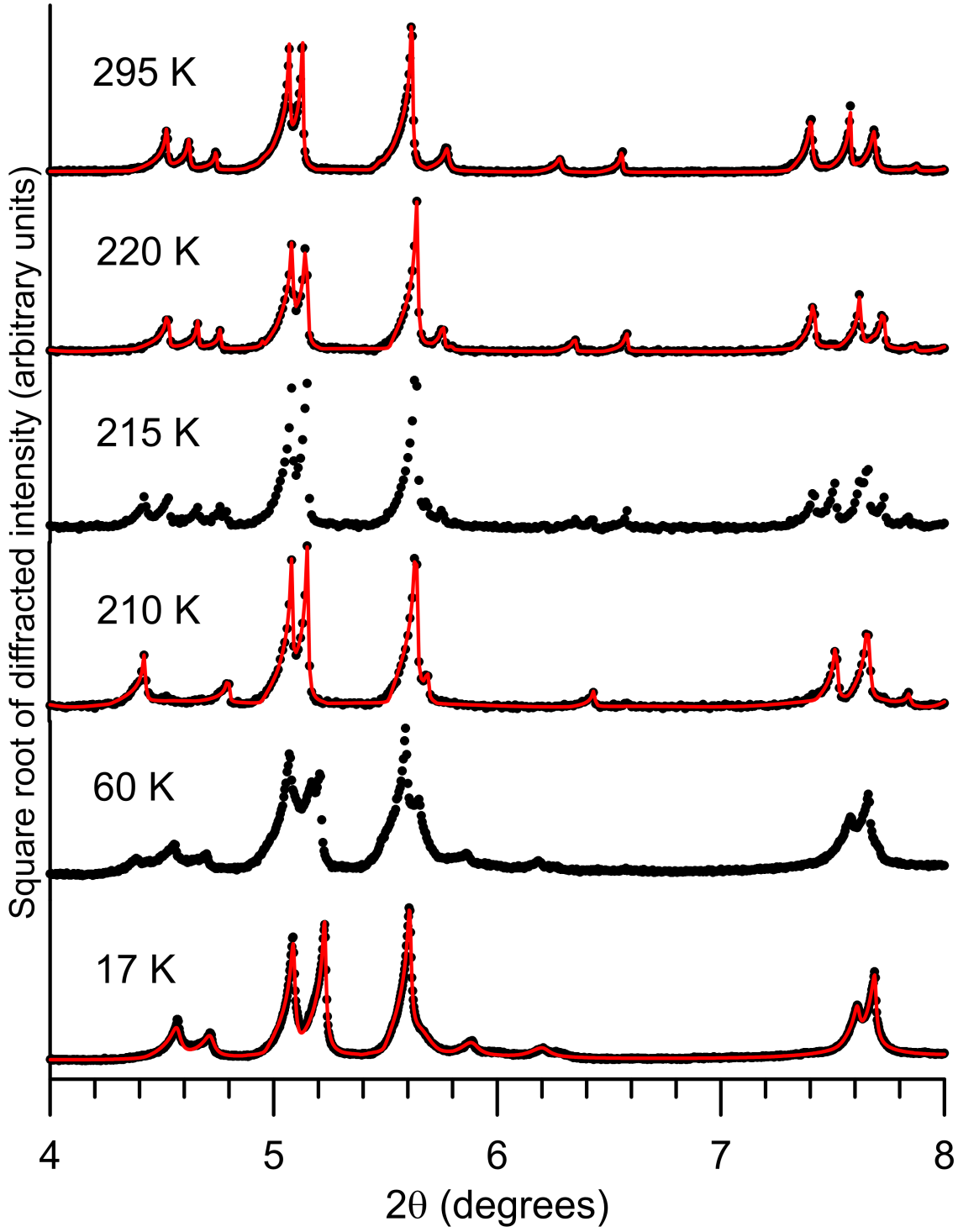

Figure S4. Powder X-ray diffraction patterns of **MM** in a limited angular range, showing the differences among the three **MM** phases. Red lines are Rietveld refinements as discussed in the text. Patterns at 215 and 60 K show clear two-phase coexistence.

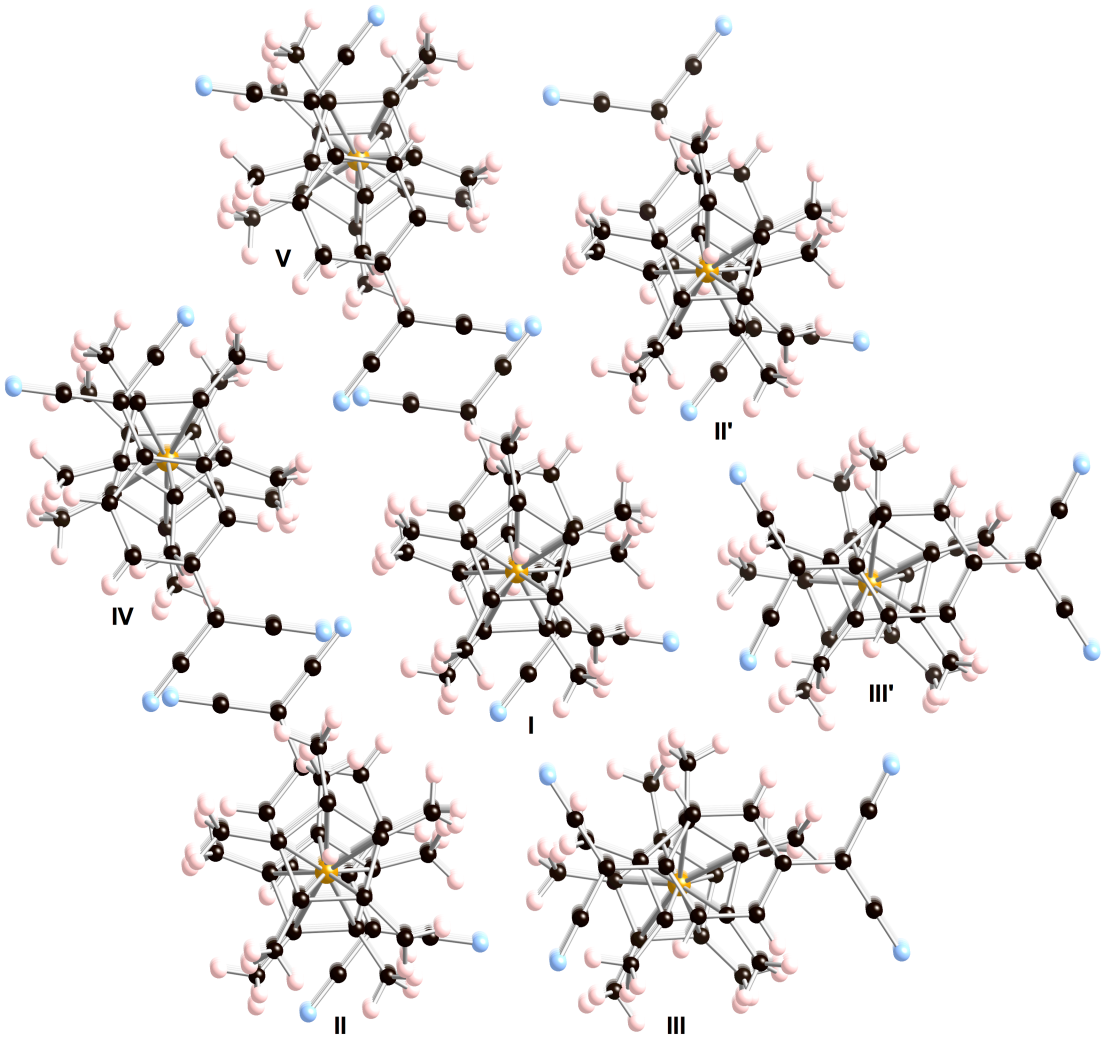

Figure S5. Nearest neighbor parallel chains **I**, **II**, **II'**, **III**, **III'**, **IV**, and **V** present in the 19-K structure of **FO**.

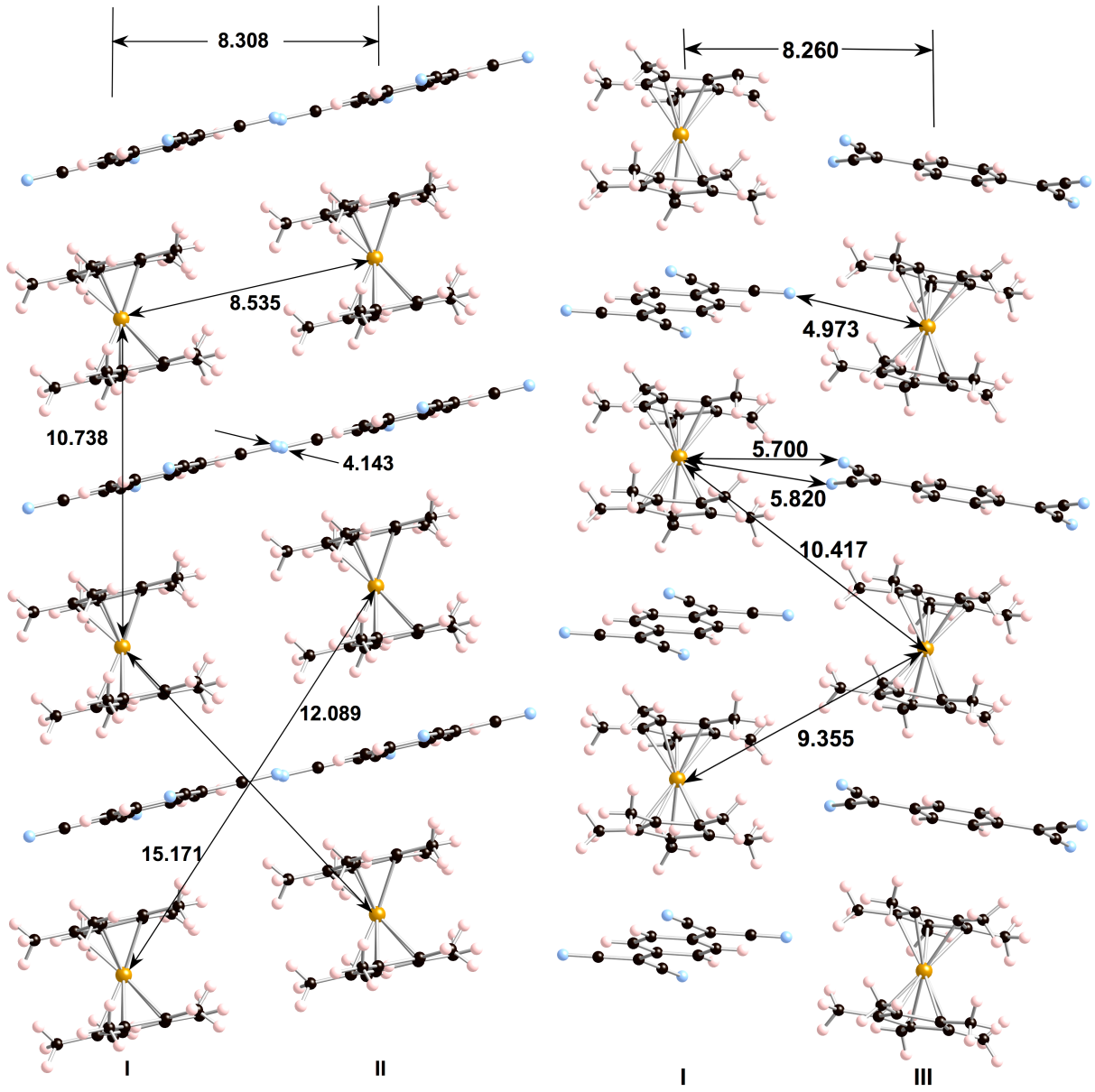
8.308
8.535
10.738
4.143
12.089
15.171
I
II
8.260
4.973
5.700
5.820
10.417
9.355
I
III

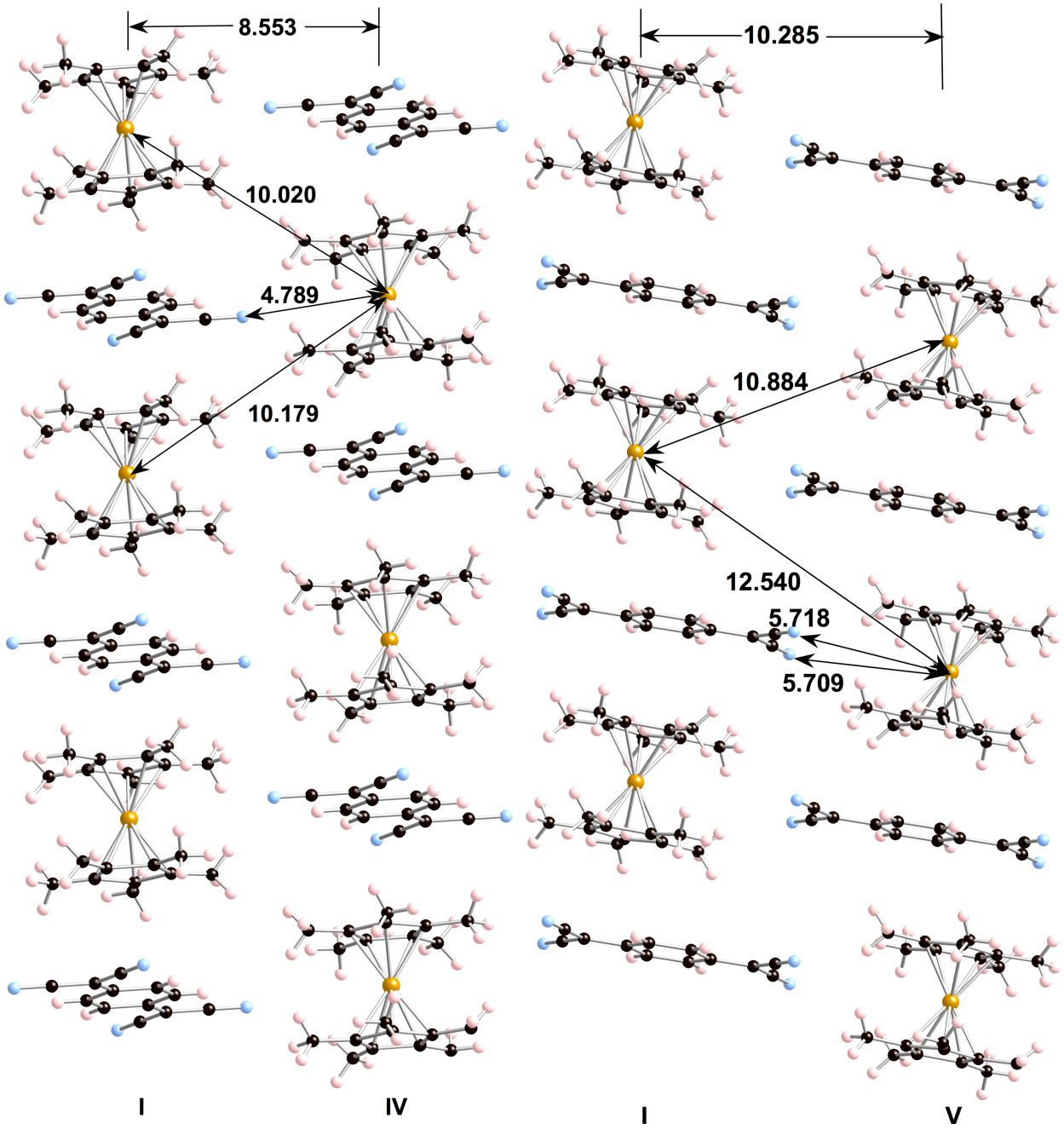

Figure S6. Nearest neighbor in-registry **I-II** (and **I-II'**), and out-of-registry **I-III** (and **I-III'**), **I-IV**, and **I-V** parallel chains present in the 19-K structure of **FO**, and the key intra- and interchain separations (Å).

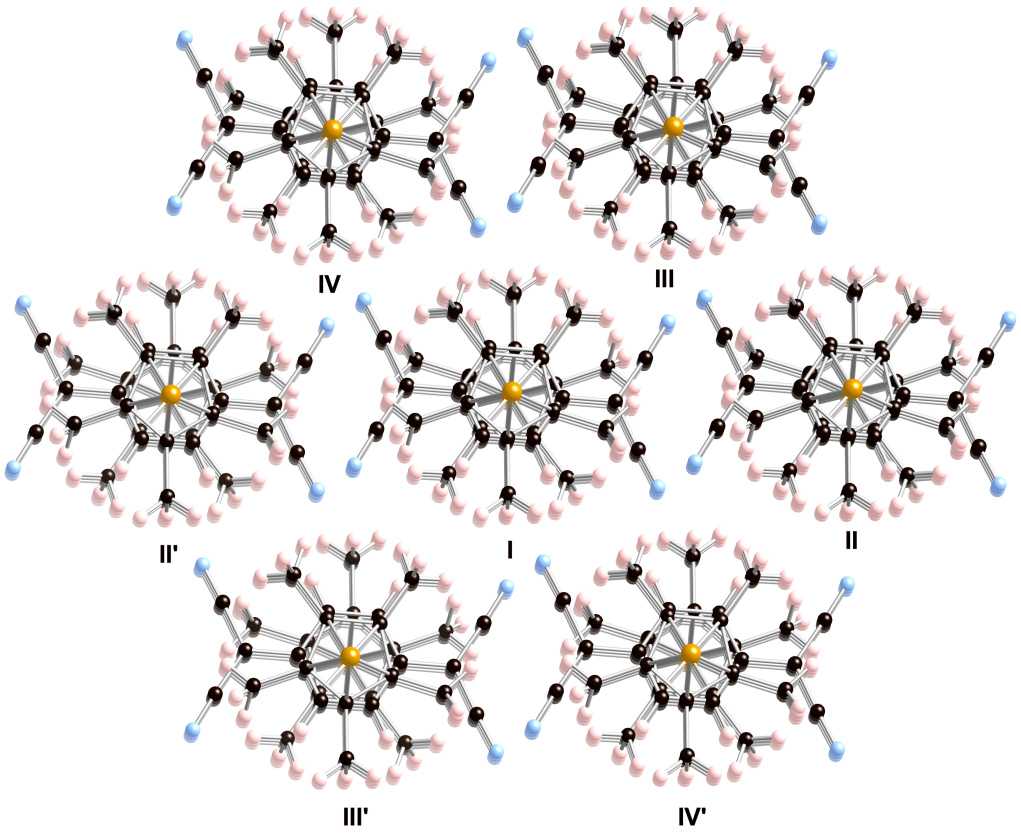

Figure S7. Nearest neighbor parallel chains **I**, **II**, **II'**, **III**, **III'**, **IV**, and **IV'** present in the 17-K structure of $\mathbf{MM_{LT}}$.

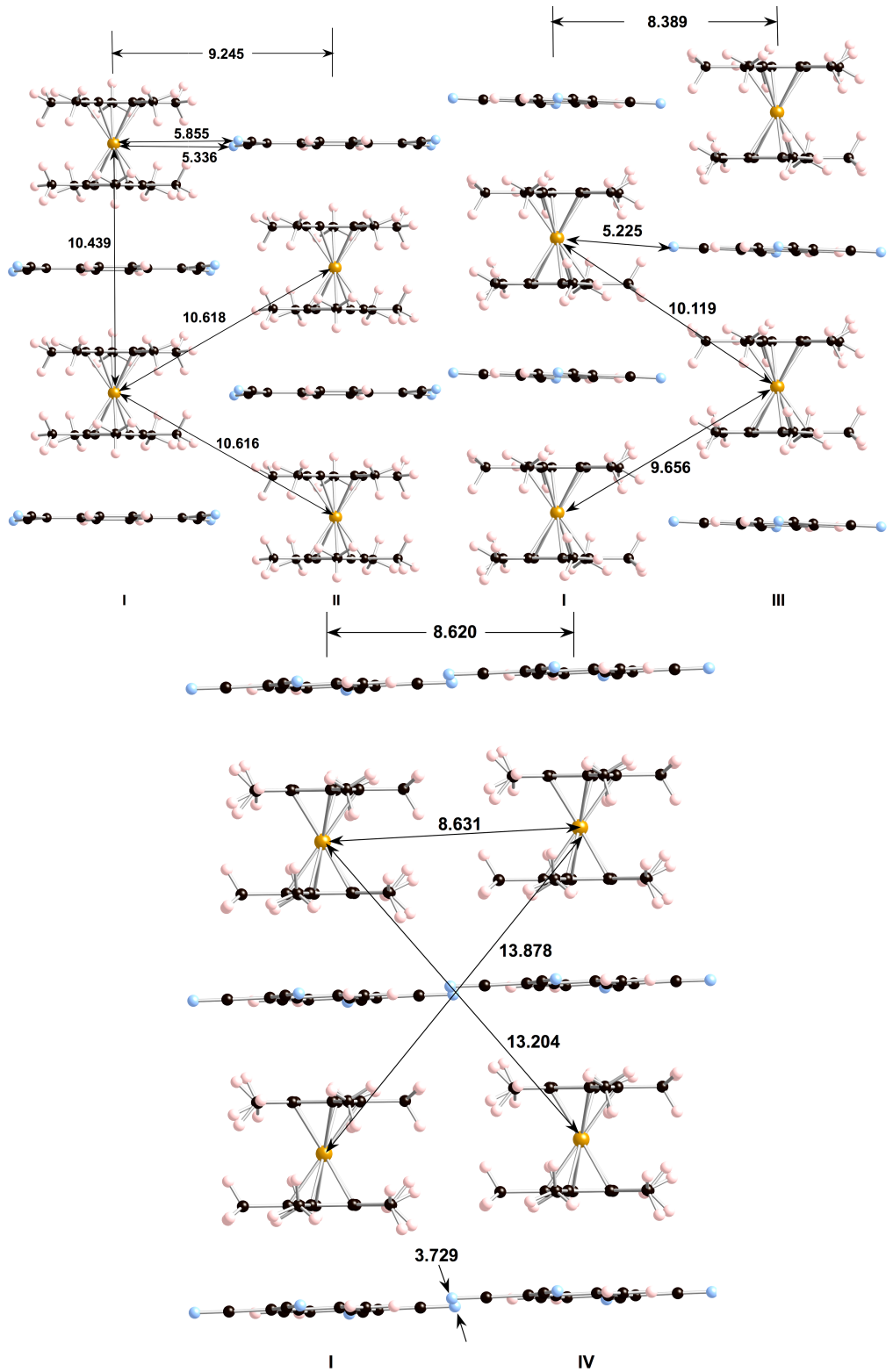

Figure S8. Nearest neighbor out-of-registry **I-II** (and **I-II'**) and **I-III** (and **I-III'**) as well as in-registry **I-IV** (and **I-IV'**) parallel chains present in the 17-K structure of $\mathbf{MM_{LT}}$, and the key intra- and interchain separations (Å).

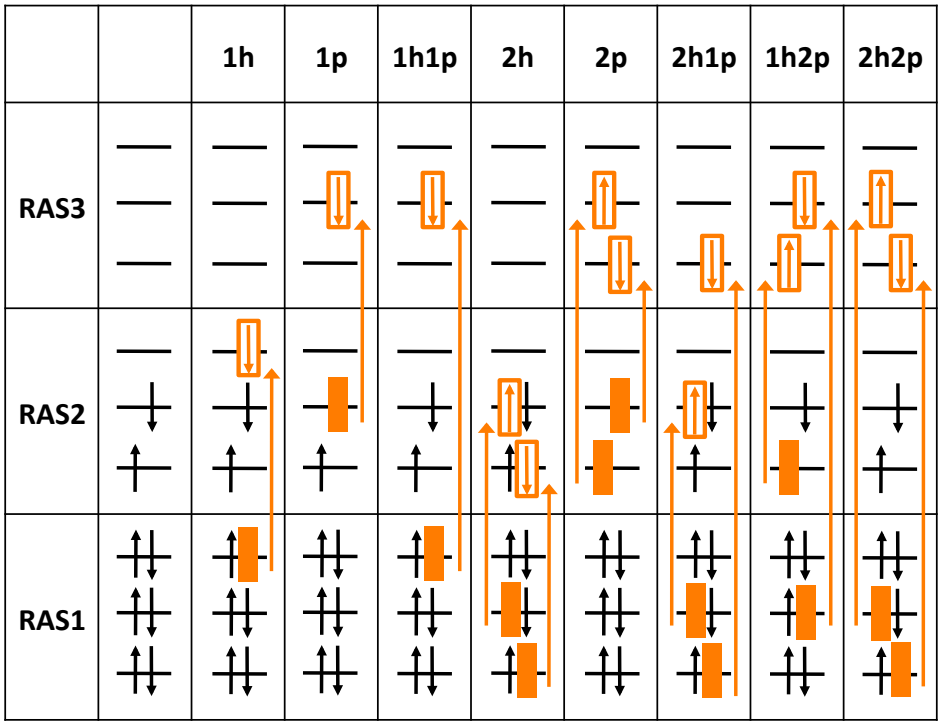

Figure S9. RAS(X, 2, 2; n1, n2, n3) space includes all possible configurations contained in RAS2 and all 1h, 1p, 1h1p, 2h, 2p, 2h1p, 1h2p and 2h2p type of excited configurations considering the RAS1 and RAS3 spaces.

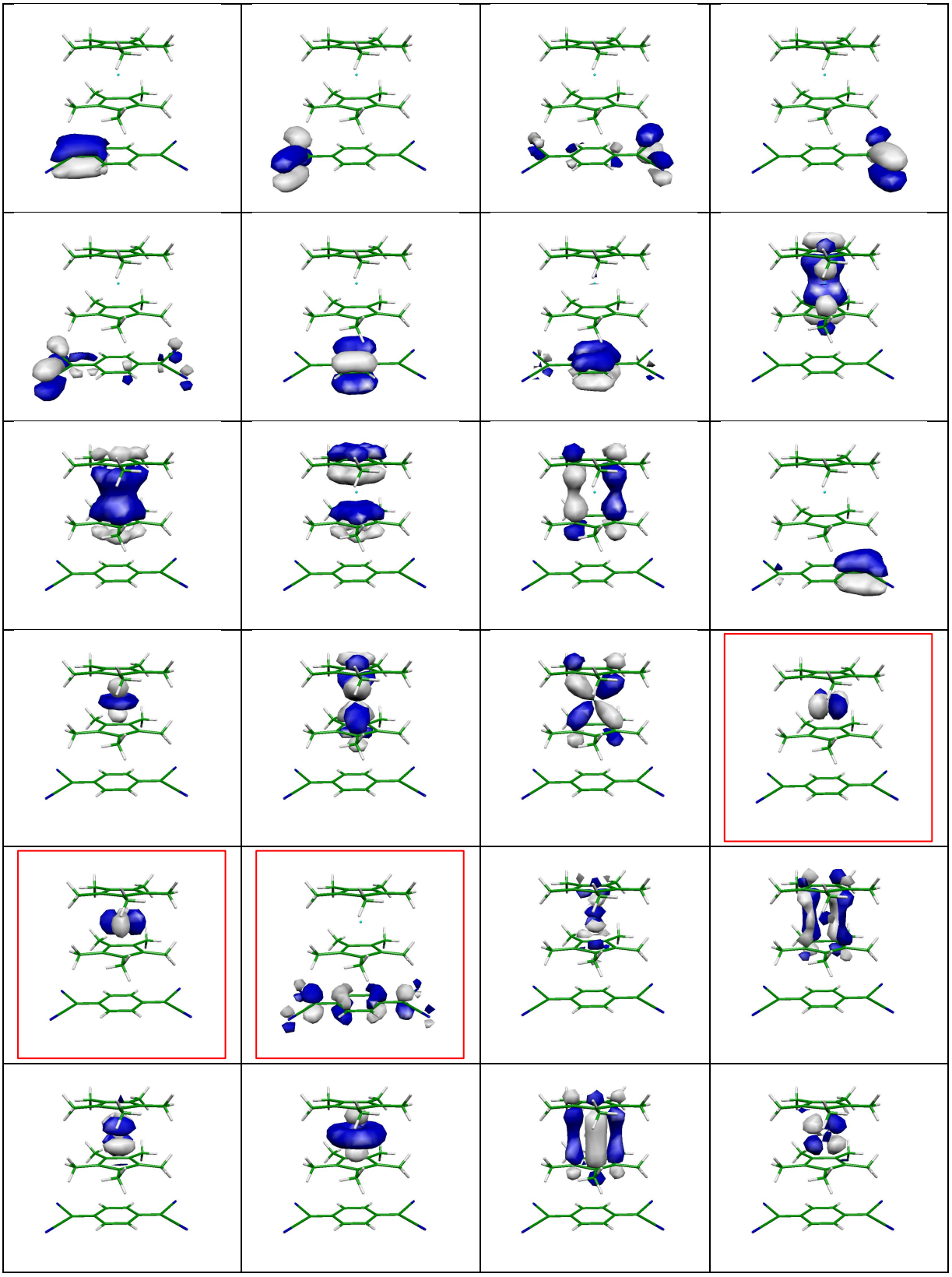

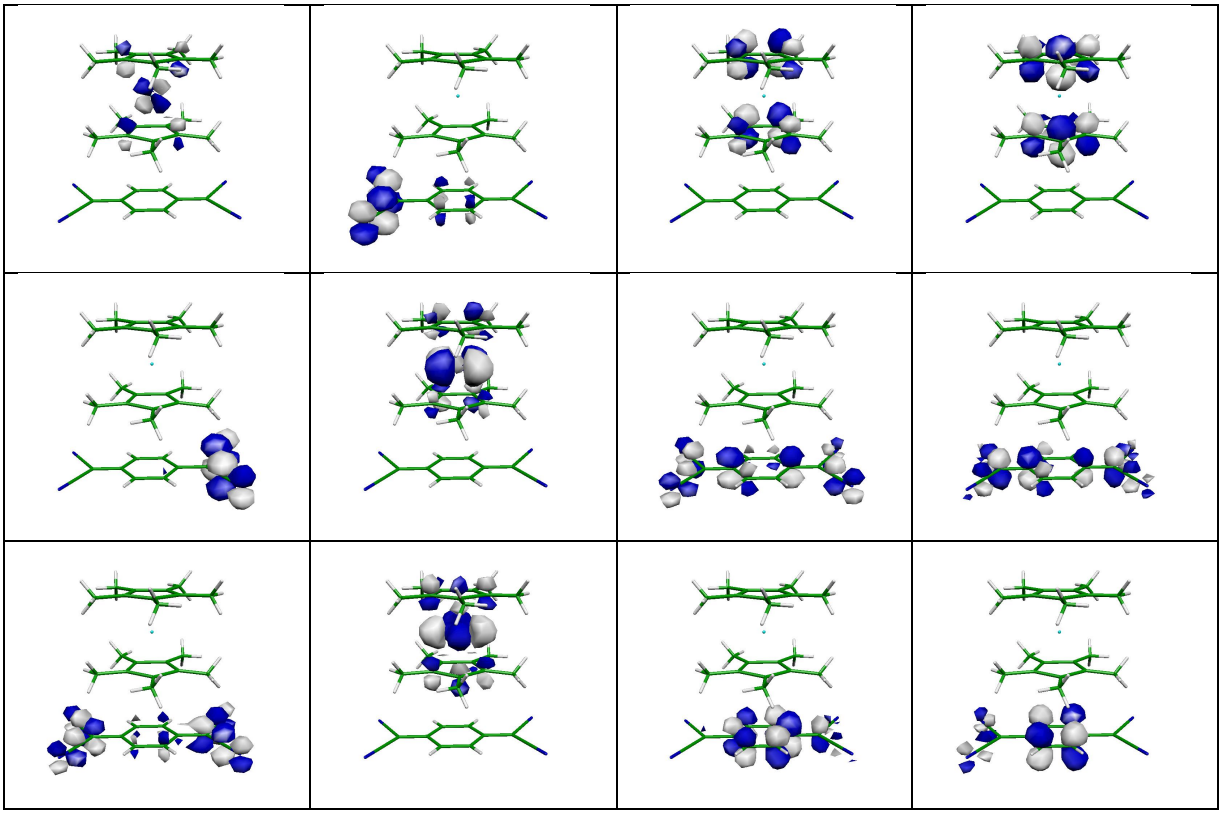

Figure S10. Active orbitals of the RAS(34,2,2;15,3,18) space used to compute the *J* values for the $[FeCp^*_2]^{\bullet+}$•••$[TCNQ]^{\bullet-}$ pairs. The 3 orbitals placed inside red squares are the orbitals included in the RAS2 subspace, while the 15 above are the RAS1 and the 18 below the RAS3 subspaces. As shown in Figure S9, the orbitals and electrons included in RAS2 give rise to the same type of full-CI expansion as in a Complete Active Space (CAS) calculation.

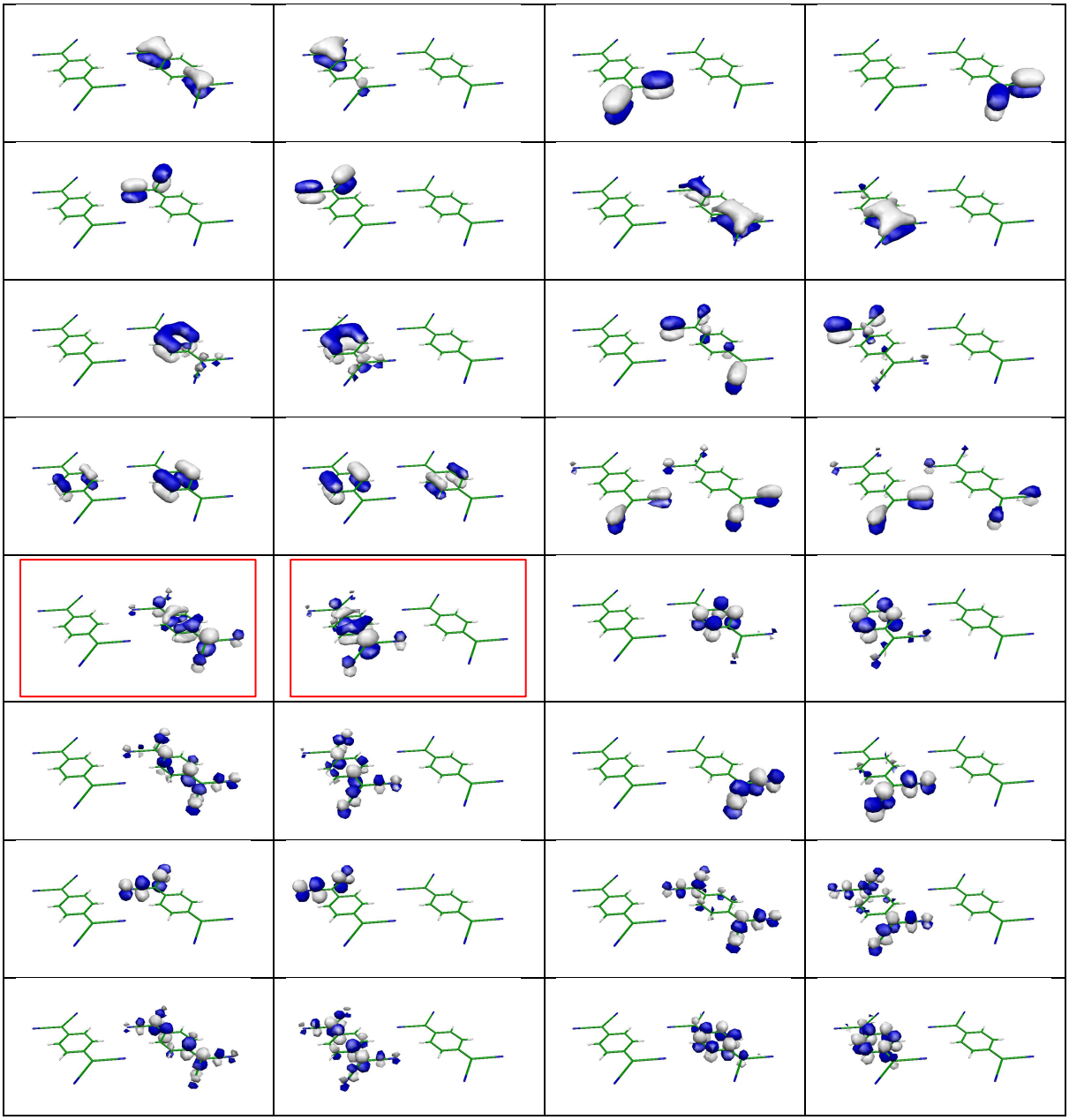

Figure S11. Active orbitals of the RAS(34,2,2;16,2,14) space used to compute the *J* values for the $[TCNQ]^{-\bullet}$•••$[TCNQ]^{-\bullet}$ pairs. The 3 orbitals placed inside red squares are the orbitals included in the RAS2 subspace, while the 16 above are the RAS1 and the 14 below the RAS3 subspaces. As shown in Figure S9, the orbitals and electrons included in RAS2 give rise to the same type of full-CI expansion as in a Complete Active Space (CAS) calculation.

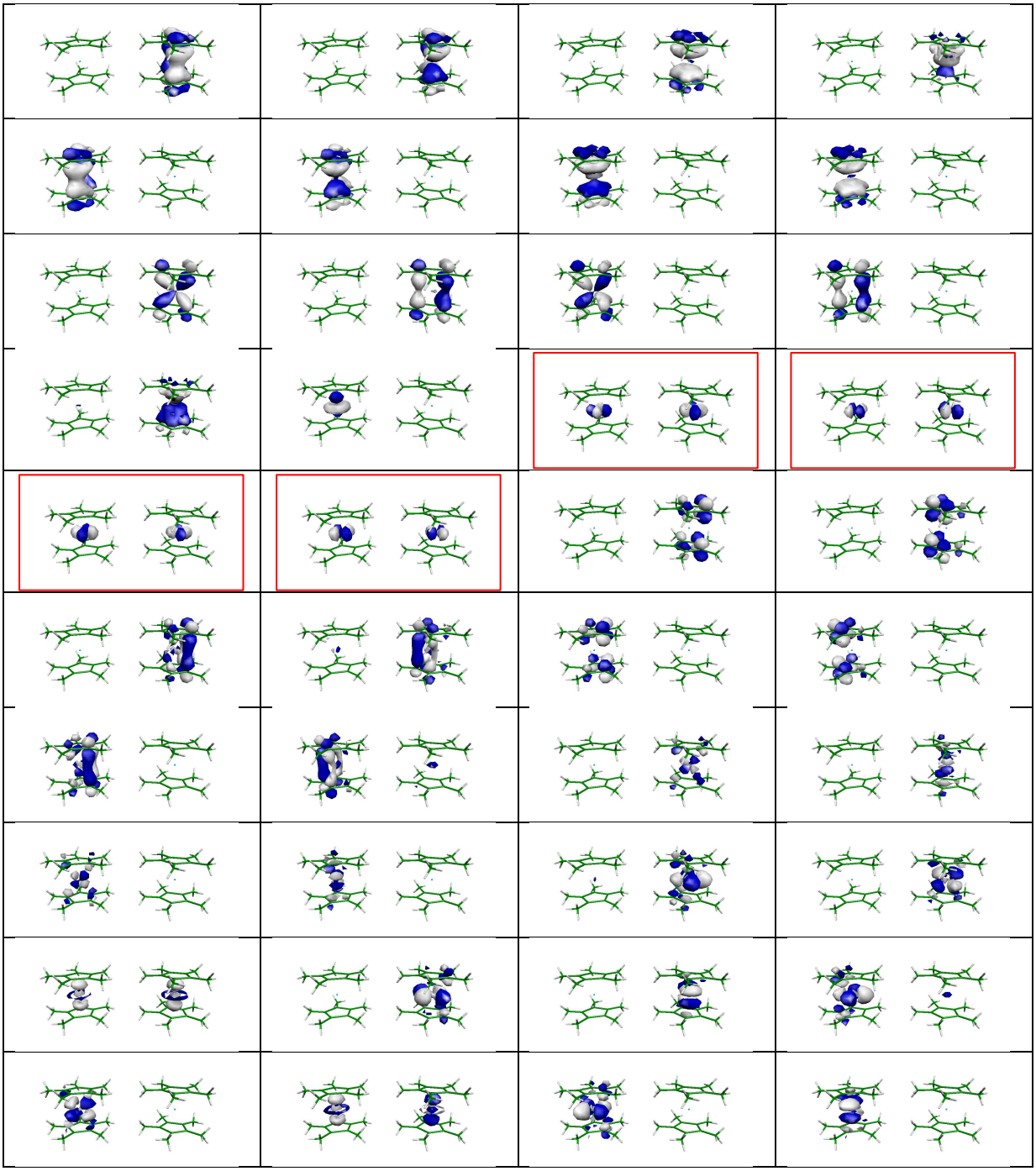

Figure S12. Active orbitals of the RAS(34,2,2;14,4,22) space used to compute the *J* values for the $[FeCp^*_2]^{\bullet+}$•••$[FeCp^*_2]^{\bullet+}$ pairs. The 4 orbitals placed inside red squares are the orbitals included in the RAS2 subspace while the 14 above are the RAS1 and the 22 below the RAS3 subspaces. As shown in Figure S9, the orbitals and electrons included in RAS2 give rise to the same type of full-CI expansion as in a Complete Active Space (CAS) calculation.

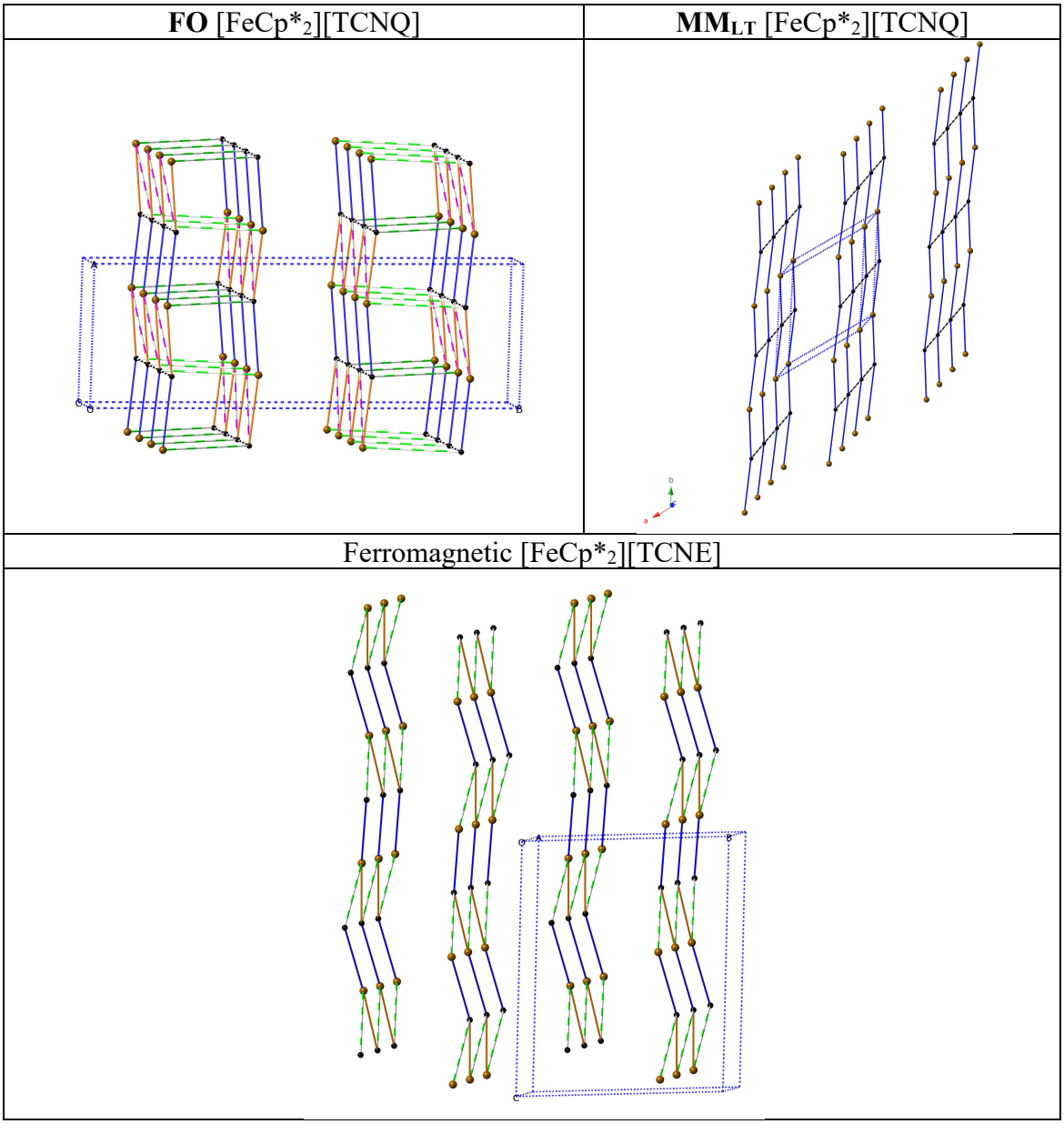

Figure S13. Magnetic topologies of [FeCp*$_2$][TCNE] and **FO** and **MM$_{LT}$** polymorphs of [FeCp*$_2$][TCNQ]. A unit cell is depicted by the dashed blue lines.